AGU PUBLICATIONS

Space Weather

RESEARCH ARTICLE
10.1002/2014SW001147

Key Points:
- We quantify the electron environment before 26 amplifier anomalies
- Anomalies occur more often when electron fluence over 14–21 days is elevated
- The e field 14–21 days before the anomalies can cause breakdown of coax cables

Correspondence to:
W. Lohmeyer,
whitneylohmeyer@gmail.com

Citation:
Lohmeyer, W., A. Carlton, F. Wong, M. Bodeau, A. Kennedy, and K. Cahoy (2015), Response of geostationary communications satellite solid-state power amplifiers to high-energy electron fluence, *Space Weather*, *13*, 298–315, doi:10.1002/2014SW001147.

Received 17 NOV 2014
Accepted 2 APR 2015
Accepted article online 9 APR 2015
Published online 25 MAY 2015

Response of geostationary communications satellite solid-state power amplifiers to high-energy electron fluence

Whitney Lohmeyer[1], Ashley Carlton[1], Frankie Wong[2], Michael Bodeau[3], Andrew Kennedy[1], and Kerri Cahoy[1]

[1]MIT Aeronautics and Astronautics, Cambridge, Massachusetts, USA, [2]Space Systems Loral, Palo Alto, California, USA, [3]Northrop Grumman, Redondo Beach, California, USA

Abstract The key components in communications satellite payloads are the high-power amplifiers that amplify the received signal so that it can be accurately transmitted to the intended end user. In this study, we examine 26 amplifier anomalies and quantify the high-energy electron environment for periods of time prior to the anomalies. Building on the work of Lohmeyer and Cahoy (2013), we find that anomalies occur at a rate higher than just by chance when the >2 MeV electron fluence accumulated over 14 and 21 days is elevated. To try to understand "why," we model the amplifier subsystem to assess whether the dielectric material in the radio frequency (RF) coaxial cables, which are the most exposed part of the system, is liable to experience electrical breakdown due to internal charging. We find that the accumulated electric field over the 14 and 21 days leading up to the anomalies is high enough to cause the dielectric material in the coax to breakdown. We also find that the accumulated voltages reached are high enough to compromise components in the amplifier system, for example, the direct current (DC) blocking capacitor. An electron beam test using a representative coaxial cable terminated in a blocking capacitor showed that discharges could occur with peak voltages and energies sufficient to damage active RF semiconductor devices.

1. Introduction

The purpose of this work is to expand upon the *Lohmeyer and Cahoy* [2013] analysis of 665,112 operational hours of archived geostationary communications satellite telemetry from Inmarsat, a telecommunications satellite operator based in the UK. In the previous work, power amplifier current measurements and anomaly logs for two separate satellite fleets, Fleet A and Fleet B, were considered. These two satellite fleets consisted of eight satellites equipped with a combined total of more than 450 RF power amplifiers. Between 1996 and 2012, 26 amplifier anomalies occurred.

RF power amplifiers are key components on board communications satellites. Commonly, communication systems have a "bent-pipe" configuration [*Roddy*, 2001]. In a bent-pipe configuration, the ground signal is received and amplified with a low-noise amplifier (LNA), which increases the strength of the signal after it experiences losses during uplink (free-space path loss, transmission line loss, polarization loss, etc.). The signal frequency is then converted from the receive frequency to the transmit frequency with a downconverter/upconverter, which is then followed by an RF power amplifier. Solid-state power amplifiers (SSPAs) and traveling wave tube amplifiers are the two most common types of RF power amplifiers for communication satellite systems. The power amplifier boosts the power of the signal to a level high enough to be retransmitted and detected. The amplifiers on board Fleet A and Fleet B were all SSPAs.

As described in *Lohmeyer and Cahoy* [2013], component performance anomalies occur when operating parameters exceed specified thresholds. Hard failures occur when the component is not recoverable after exceeding such thresholds; thus, necessitating the use of a redundant amplifier. Soft failures occur when thresholds are exceeded, but operation of the same amplifier can continue without the use of a redundant amplifier.

Four of the amplifier anomalies were soft; however, only one of the four failures was ultimately able to continue operating, resulting in 25 of 26 failures as hard amplifier failures. The telemetry data indicated that the hard failures manifested as a drop in the SSPA RF current, without a change in the DC power supply or in the command and telemetry functionality, which points to the RF circuitry as the location of the failures.

Inmarsat has not had any notable service interruptions due to SSPA anomalies, due to the availability of redundant units. Inmarsat currently has 690 SSPAs flying with a total of >6300 operational years. The observed failure rate of 0.004 per SSPA per year is far better than the original system design requirements within the general industry standards; and as such, the performance of the payloads remains highly resilient. It is also important to note that Inmarsat has led the field by providing the authors with access to some of their telemetry data for in-depth analysis. Inmarsat's support of the goal to learn as much as possible about the operational environment has enabled studies like this one to more meaningfully probe root causes and sensitivities in ways that will improve understanding for future applications.

1.1. Previous Findings of *Lohmeyer and Cahoy* [2013]

Lohmeyer and Cahoy [2013] compared SSPA current measurements for the 26 anomalous power amplifiers to space weather data: *Kp* index, high-energy electron flux, and sunspot number. The local time of the satellite at the time of amplifier failure was also considered, since surface charging induced anomalies cluster in the midnight-to-dawn local time quadrant. The authors concluded that surface charging was not the sole failure mechanism of the SSPAs after analyzing both the *Kp* index, which was used as a proxy for surface charging, and analyzing the local time at which the anomalies occurred. Additionally, the location of the SSPAs deep within the spacecraft structure and the fact that the coaxial cables connecting to the RF input and output circuits shield against external electromagnetic disturbances reduce the likelihood of failure due to surface charging.

More than 69% of the 13 anomalies from Fleet A occurred during the declining phase of the solar cycle. The declining phase is known for corotating interaction regions and associated high-speed solar wind streams, which cause an enhanced relativistic electron environment that increases the likelihood of internal charging [*Shea and Smart*, 1998; *Denton et al.,* 2006; *Miyoshi and Kataoka,* 2008]. Fleet A was launched during the ascending phase, when energetic electron flux tends to be lower. The first anomaly occurred in Fleet A 3 years after launch. Fleet B has yet to operate for a complete solar cycle, so conclusions pertaining to the relative rate of occurrence of anomalies throughout the solar cycle cannot be made.

1.2. Internal Charging Analysis Motivation

Internal (or bulk) charging occurs when high-energy particles (e.g., MeV electrons) penetrate satellite shielding materials and deposit charge on internal spacecraft components. If the component's resistivity is high (e.g., $>1\times10^{18}$ ohm cm for Teflon), the rate of charge buildup can overcome the rate of charge leakage from the material during periods of high flux [e.g., *Wrenn,* 1995; *Lai*, 2012]. The accumulated charge and associated induced electric field may then exceed the breakdown threshold for the material, causing electrostatic discharges (ESDs) in the insulating material [e.g., *Reagan et al.,* 1983; *Baker*, 2000; *Fennell et al.,* 2001; *Bodeau*, 2010]. The resulting discharge is potentially hazardous directly to the material, or indirectly to other spacecraft components, causing spacecraft component anomalies.

In the *Lohmeyer and Cahoy* [2013] studied anomalies occurring between 7 and 14 days following high-energy electron events (defined as having a peak electron flux in the 1.8–3.5 MeV range greater than 1.5 standard deviations above the average). For the events with available 1.8–3.5 MeV flux observations at the time of the amplifier anomalies, they found that 29% (6 out of 21) of the anomalies occurred in the 7–14 day window following high-energy electron events, compared to an occurrence rate of only 13.3% for randomly selected events found with a Monte Carlo simulation. Thus, the Monte Carlo simulation suggested that the number of anomalies that occur following high-energy electron events was statistically greater than expected. This result agrees with statistical correlations of anomalies with high-energy electron flux performed by others [*Balcewicz et al.,* 1998, and references cited in *Bodeau*, 2010].

The statistics suggest that a more thorough examination of the high-energy electron fluence experienced before the anomalies is warranted to determine if internal charging served as a likely failure mechanism [*Bodeau*, 2010]. Therefore, in this study, we determine the high-energy electron fluence over periods of 1, 3, 7, 10, 14, and 21 days prior to the anomalies versus examining just the peak flux during those time periods as was done in the *Lohmeyer and Cahoy* [2013] study. In section 2 we confirm that the SSPA anomalies cluster at a higher than expected rate when >2 MeV electron fluence for 14 and 21 days prior to the anomalies was high compared to all >2 MeV electron fluence measurements for similar durations in

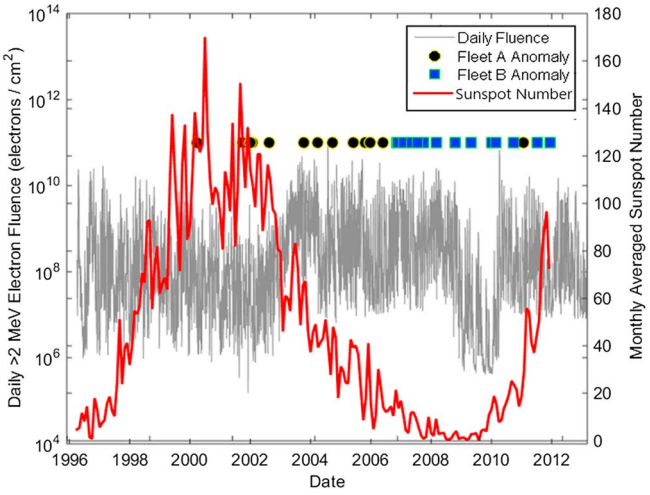

Figure 1. Daily >2 MeV electron fluence and the time of SSPA anomalies. Fleet A anomalies are marked with a black circle outlined in yellow, and Fleet B anomalies are marked with a blue square outlined in green. The GOES daily 2 MeV electron fluence, marked in gray, spans between 1996 and 2012, and the solar cycle is shown in red.

the 1996–2012 interval. A Monte Carlo analysis conducted on daily >2 MeV electron fluence measurements shows a higher rate of occurrence of anomalies after high fluence than expected by chance.

In section 3, the components of the amplifier system are outlined and the important ones highlighted. Section 4 details the internal charging analysis using European Space Agency's (ESA) internal charging model, Dielectric Internal Charging Threat Analysis Tool (DICTAT) [*Rodgers,* 2004]. DICTAT is used to assess whether internal charging is indeed a possible and likely amplifier failure mechanism by parametrically modeling 35 different combinations of six material resistivities (taken at room temperature) and seven temperatures. Having established that coax charging and ESD was plausible for a subset of *assumed* temperatures and coax insulation resistivities (taken at room temperature), tests were performed to determine if ESD was plausible for real coax cables. Section 5 describes the experimental setup, electron beam testing, and results of amplifier components in a simulated worst-case GEO environment. In section 6, the results of this study are summarized and discussed.

2. Analysis of GOES >2 MeV Electron Fluence and SSPA Anomalies

In this work, we used continuous GOES daily >2 MeV electron fluence data (http://www.swpc.noaa.gov/ftpmenu/indices/old_indices_html) from 1996 to 2012 to quantify the fluence prior to the anomalies. Figure 1 shows the GOES >2 MeV daily electron fluence measurements from 1996 to 2012, the 11 year Sunspot cycle, and the times at which the SSPA anomalies occurred. Fleet A and Fleet B were not launched simultaneously; exact launch dates are not discussed in detail for proprietary reasons. However, it is important to note that Fleet A was in operation as early as 1996 and did not experience any SSPA failures until year three of operation. The fleet on which the anomalies occurred is indicated, but the vertical location designates a generic >2 MeV electron fluence.

As previously mentioned, *Lohmeyer and Cahoy* [2013] found more than 69% of the 13 anomalies from Fleet A occurred during the declining phase of the solar cycle. Fleet B had yet to operate for a complete solar cycle, so analysis of anomaly occurrence throughout an entire solar cycle was not conducted. The lack of apparent correlation of anomaly occurrence and daily high-energy electron fluence shown in Figure 1 does not clearly indicate that the anomalies are driven by energetic electron flux over a particular day but motivates the investigation of more persistent flux over longer periods of time prior to the anomaly.

Two sets of design criteria for ESD hazards have been established. First and most commonly cited is the *NASA-HDBK-4002A* [2011] criterion; the second is defined in *Wrenn and Smith* [1996]. The NASA handbook specifies a safe *10 h* fluence level of $\leq 2 \times 10^{10}$ el/cm^2. The safe-fluence level is derived from the Combined Release and Radiation Effects Satellite (CRRES) Internal Discharge Monitor (IDM), which experienced no ESD events when the accumulated fluence *inside the IDM* over a 10 h orbit was less than 2×10^{10} el/cm^2 [*Vampola,* 1987]. The safe 10 h fluence level is not accompanied by a safe-fluence energy level, however, an analysis in *NASA-HDBK-4002A* [2011] using a suggested worst-case environment indicates that a total shielding of 110 mils aluminum equivalent thickness would reduce the fluence behind the shielding to below a safe-fluence limit.

Wrenn and Smith [1996] define two thresholds for space hazards. Threshold I states that significant probability of hazard exists when >2 MeV *daily* electron fluence *outside the spacecraft* exceeds 3.8×10^9 el/cm^2. (Note that

the NASA 4002 criterion is the fluence inside the spacecraft.) Threshold II states that an extremely significant probability of hazard exists when >2 MeV daily electron fluence exceeds 3.8×10^{10} el/cm^2 [*Lai,* 2012]. These thresholds are based upon empirical correlations of anomalies with the external electron flux data. However, we must keep in mind that the >2 MeV electron flux outside the spacecraft is only a proxy for the actual electron fluence reaching the source of ESD inside the spacecraft. The range of a 2 MeV electron is about 170 mils (4.3 mm) aluminum [*Bodeau*, 2010]. If the shielding between the ESD source and external environment is less than that, then lower energy electrons can penetrate the shielding and contribute to the charging of the ESD source. There are far more electrons at energies lower than 2 MeV, so the >2 MeV external flux level may understate the total flux of electrons reaching the ESD source if the shielding is substantially lower than 170 mils aluminum.

Bodeau [2010] found these safe-fluence levels inappropriate for materials with electrical time constants (electrical time constant equals the product of dielectric constant and resistivity), much longer than 10 h, and specified that the safe-level criterion should be based upon the fluence for an interval that reflects a material's electrical time constant. When the CRRES IDM was designed, engineering handbooks gave polytetrafluoroethylene (PTFE) Teflon a resistivity at room temperature in the 1×10^{13} to 1×10^{17} ohm cm range [*Robinson*, 1989; *Cotts and Reyes*, 1985], which would give a corresponding time constant between 1 s and 3.3 h. A 10 h fluence criterion would reflect three electrical time constants, over which time a material should approach its peak steady state voltage. So the NASA 4002 criterion appears to meet the standard set by Bodeau. However, it was subsequently established [e.g., *Swaminathan et al.,* 2003, and references therein] that the resistivity measurement techniques codified in standards such as *ASTM D-257* [2014] and derivative standards such as IEC 93 [1980] are

> "…typically instrumentation resolution limited to accurate measurements of resistivities of less than 1E + 12 to 1E + 17 Ω-cm. Inconsistencies in sample humidity, sample temperature, initial voltages and other factors from such tests cause significant variability in results. Further, the duration of standard tests are short enough that the primary currents used to determine resistivity are often caused by the polarization of molecules by the applied electric field rather than by charge transport through the bulk of the dielectric. Testing over much longer periods of time in a well-controlled vacuum environment is required to allow this polarization current to become small so that accurate observation of the more relevant charged particle transport through a dielectric material is possible."

When improved methods were applied to CRRES IDM samples, the room temperature resistivity of its PTFE was found to be around 3×10^{20} ohm cm and its electrical time constant was 339 days [*Green et al.*, 2005]. Similarly, *Green et al.* found that the electrical time constants of other materials, such as circuit board (FR4) and alumina, were orders of magnitude higher than the ASTM-based material time constants. Because the actual material time constants are so long, it is possible to accumulate sufficient charge to reach electrical breakdown from much lower average flux levels over longer time periods [*Bodeau*, 2010]. Unfortunately, because these advanced test methods have not yet been applied to most spacecraft materials, material-specific safe-fluence criteria cannot be established and a revised fluence threshold of 2×10^9 el/cm^2 has been suggested in the interim [*NASA-HDBK 4002A,* 2011]

The highest >2 MeV daily electron fluence on the days on which anomalies occurred was approximately 9×10^9 el/cm^2. None of the 26 anomalies breached the *NASA-HDBK-4002A* [2011] safe 10 h fluence level of 2×10^{10} el/cm^2 or *Wrenn and Smith's* Threshold II of 3.8×10^{10} el/cm^2. One of the 26 SSPA anomalies breached *Wrenn and Smith's* Threshold I of 3.8×10^9 el/cm^2. Five of the 26 SSPA anomalies experienced a daily >2 MeV electron fluence of greater than the more conservative interim safe 10 h fluence 2×10^9 el/cm^2 in *NASA-HDBK-4002A* [2011].

To verify that a relationship between the observed higher rate of anomalies and high fluence exists, we performed 1000 trials of 26 randomly selected days between 1996 and 2012 and quantified the distribution of 1, 3, 7, 10, 14, and 21 day fluence values prior to the 26 random dates to determine the mean fluence value as well as the standard deviation of fluences. The disproportionate distribution of anomalies in the higher-fluence intervals occurs at a rate that is not easily explained by a simple random sampling of the dates and, therefore, shows a relationship with high fluence exists.

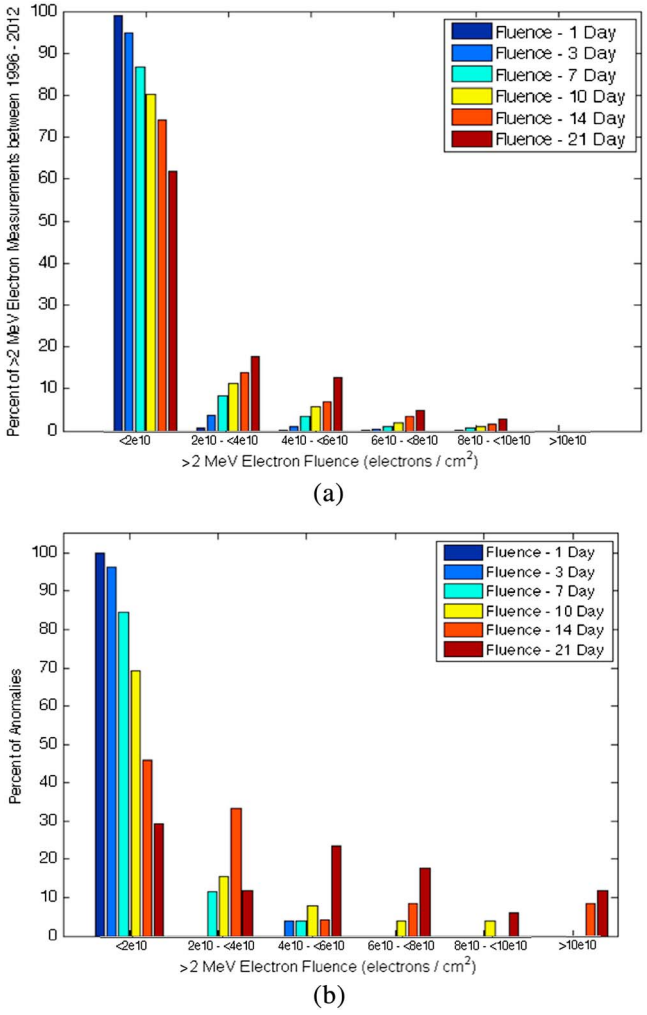

Figure 2. (a) Percentage of >2 MeV electron fluence measurements from 1996 to 2012 over periods of 1, 3, 7, 10 14, and 21 day periods, and (b) percentage of SSPA anomalies that occur for a given total >2 MeV electron fluence over periods of 1, 3, 7, 10, 14, and 21 days prior to the 26 SSPA anomalies.

2.1. Distribution of GOES >2 MeV Electron Fluence From 1996 to 2012

Figure 2a shows the distribution of the >2 MeV electron fluence from 1996 to 2012 for 1, 3, 7, 10, 14, and 21 days, and Figure 2b shows the percentage of anomalies that occurred at a particular GOES >2 MeV electron fluence for the 1, 3, 7, 10, 14, and 21 day periods of interest. The fluence bins are differential bins: $<2\times10^{10}$ el/cm^2, $2–4\times10^{10}$ el/cm^2, $4–6\times10^{10}$ el/cm^2, $6–8\times10^{10}$ el/cm^2, and $>10\times10^{10}$ el/cm^2.

It is important to note that the longer fluence periods (7, 14, and 21 days) at the same fluence interval, for example 2×10^{10} to 4×10^{10} el/cm^2, specify lower average daily fluxes. No fluence measurements exceeded 1×10^{11} el/cm^2. Of the 6180 total daily >2 MeV electron fluence measurements, 99% were between 0 and 2×10^{10} el/cm^2. Similarly, the majority of >2 MeV electron fluence measurements for the 3, 7, 10, 14, and 21 day periods were within the same limits. A total of 49 out of 350, or 14%, of the >2 MeV 14 day electron fluence measurements were in the next higher-fluence bin, $(2–4\times10^{10})$ el/cm^2. A total of 13% of >2 MeV 21 day electron fluence measurements occurred in the third fluence bin ($4–6\times10^{10}$ el/cm^2) and 3% occurred in the fourth bin ($6–8\times10^{10}$ el/cm^2). Given this baseline distribution, when we next examine the SSPA failures, if the SSPA failures were random and unrelated to the environment, we would expect the percentile distribution of failures with fluence to look like the percentile distribution of the fluences themselves.

All 26 anomalies experienced a daily >2 MeV electron fluence between 0 and 2×10^{10} el/cm^2 1 day prior to the anomaly. Unfortunately, >2 MeV electron fluence measurements were not available for all periods of 14 and 21 days prior to the 26 anomalies (GOES electron data history has infrequent gaps of one or more days). Of the population of 26 anomalies, 24 have corresponding 14 day >2 MeV electron fluence measurements, and 17 have 21 day >2 MeV electron fluence measurements prior to anomalies.

Looking at the distribution of anomalies for different durations of high electron fluence prior to anomalies, we find that a disproportionate number of anomalies occur after 14 days of elevated electron fluence: e.g., the height of the 14 day bar in the second fluence bin $(2–4\times10^{10})$ of Figure 2b is much higher than the 14 day bar in the same fluence bin in Figure 2a. On the other hand, the 14 day bar in the first low-fluence bin $(<2\times10^{10})$ of Figure 2b is smaller than the 14 day bar in the same fluence bin of Figure 2a. Specifically, Figure 2b shows that 33% (8 of 24) with available data occurred with a >2 MeV 14 day electron fluence of 2E-4×10^{10} el/cm^2, compared to 14% of all measurements shown in Figure 2a in the same fluence bin.

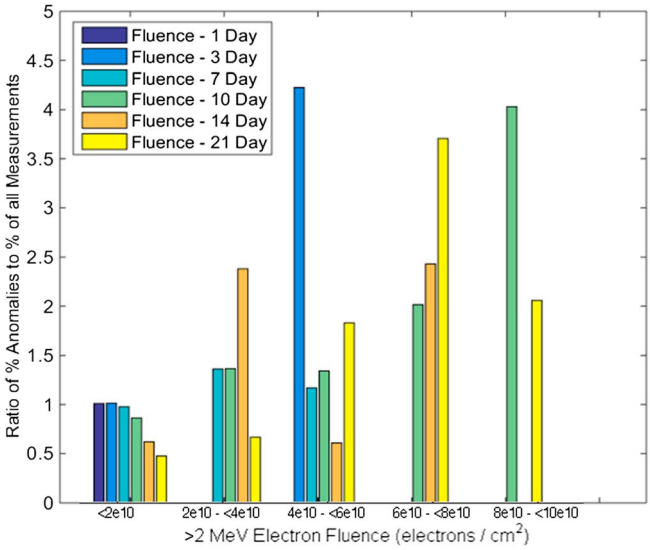

Figure 3. Ratio of the anomaly percent from Figure 2b to the measurement percent shown in Figure 2a for each >2 MeV electron fluence and each time period (1, 3, 7, 10, 14, and 21 days).

Figure 3 shows the ratio of the percentage of anomalies that occur in each fluence bin for each time period (shown in Figure 2b) to the percentage of all measurements between 1996 and 2012 for the same fluence bin and time period (shown in Figure 2a). Figure 3 shows that the rate for anomalies with a >2 MeV 14 day electron fluence of $2–4\times10^{10}$ el/cm^2 is a factor of ~2.4 times higher (33%/14%) than explainable by random failures (i.e., by the frequency of occurrence for the 14 day fluence in the same bin).

Similarly, a disproportionate percentage of anomalies occur after 21 days of elevated fluence. Of the 17 anomalies with available 21 day fluence measurements, Figure 2b shows that 23.5% of anomalies occurred with a >2 MeV 21 day fluence between 4×10^{10} and 6×10^{10} el/cm^2, compared to 13% of all >2 MeV 21 day electron fluence measurements between 1996 and 2012 in the same fluence bin, shown in Figure 2a. An additional 18% (3 of 17 anomalies) occurred with a fluence between in the third bin ($6–8\times10^{10}$ el/cm^2), which is a factor of 3.7 higher than the 4.8% of all >2 MeV 21 day fluence measurements in the same fluence bin.

Other than for the 3 day fluence period between 4×10^{10} and $<6\times10^{10}$ el/cm^2, the >2 MeV electron fluence for periods of 1, 3, and 7 days prior to the anomalies shows approximately the same proportion of anomalies that experience $<2\times10^{10}$ el/cm^2, showing no clear relationship to the environment.

2.2. Distribution of GOES >2 MeV Electron Fluence for 1000 Trials of 26 Random Days Between 1996 and 2012

To determine the likelihood of the distribution presented in Figure 2a, 26 random "anomaly dates" were selected 1000 times and the >2 MeV electron fluence over the six periods prior to the anomalies was quantified. Figure 4 shows the average percentages of the cumulative fluences compared for 26 random dates within a given >2 MeV electron fluence interval. The error bars represent a standard deviation (σ) above and below the average for the 1000 trials.

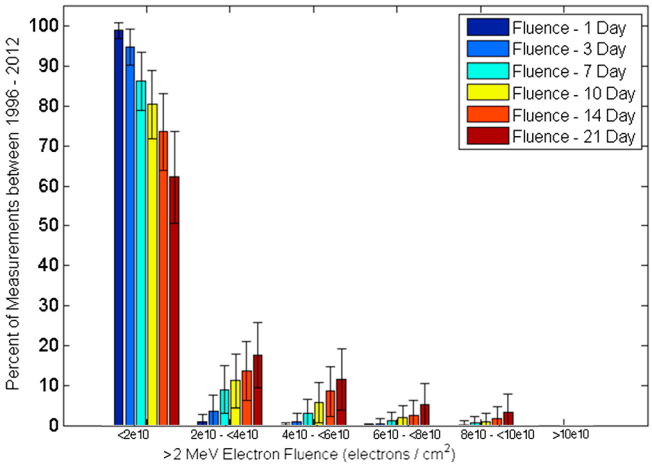

Figure 4. Percentage of 1000 random trials of 26 random days that occurred for a given >2 MeV electron fluence of 1, 3, 7, 10, 14, and 21 days prior to the randomly selected 26 days.

As expected, the distribution of values from the Monte Carlo simulation (Figure 4) are similar to distribution of the >2 MeV electron fluence measurements in Figure 2a in all fluence intervals and for all durations. For example, the percentage of measurements with a 14 day fluence in the 2×10^{10} to 4×10^{10} el/cm^2 bin is 14% (in Figure 2a) and is 13.6% in Figure 4. The standard deviation for the percentage of the 26 randomly chosen dates with 14 day fluence in the second 2×10^{10} to 4×10^{10} el/cm^2

Table 1. The Observed Anomaly Rates (%) Expressed as a Number of Standard Deviations From the Mean Value of the Monte Carlo Simulation[a]

	1 Day	3 Days	7 Days	10 Days	14 Days	21 Days
$<2\times10^{10}$	0.50	0.30	−0.23	−1.31	−2.85	−2.85
$2–<4\times10^{10}$	−0.48	−0.91	0.42	0.63	**2.62**	−0.71
$4–<6\times10^{10}$	−0.14	1.35	0.23	0.41	−0.69	**1.55**
$6–<8\times10^{10}$	−0.11	−0.31	−0.48	0.67	**1.58**	**2.34**
$8–<10\times10^{10}$	0.00	−0.23	−0.38	**1.42**	−0.60	0.58

[a]Bolded items show values that were greater than 1.4 standard deviations above the mean value of the Monte Carlo simulation.

bin was 7.5% for the 1000 trials. The observed 33.3% of SSPA failures that occurred with a 14 day fluence in the same bin is 2.62 σ higher than the mean [(33.3%–14%)/7.5%], indicating that the higher anomaly rate is not likely due to chance.

Table 1 tabulates the observed anomaly rates (%) expressed as a number of standard deviations from the mean, which shows where the rates are unusually high and unlikely to be produced by a random failure process.

Unexpected increases in observed failure rate were also compared to the Monte Carlo analysis for elevated periods of 21 day fluences before an anomaly. Focusing on the 21 day fluence events, we find that, for the third fluence bin (4×10^{10} and 6×10^{10} el/cm^2), an average of 11.6% ± 7.68% of randomly selected anomalies experienced a >2 MeV electron fluence prior to the anomalies.. The 24% (4 of 17) of anomalies with 21 day electron fluence in the same bin is 1.55 σ higher than the expected rate for a random sample of dates. An average of 5.25% ± 5.3% of the randomly selected dates experienced a >2 MeV electron fluence in the fourth fluence bin (6×10^{10} to 8×10^{10} el/cm^2). The 18% (3 of 17) of anomalies in the same fluence bin is 2.34 σ above the expected rate for a random sample of dates. Thus, the anomaly rates for long-duration, high fluence levels are higher than expected and cannot be reasonably explained by chance alone.

Based on similar statistical evidence showing a correlation of anomalies to high fluences over 14 and 21 day periods [*Balcewicz et al.*, 1998], *Bodeau* [2010] performed a real-time analysis of the accumulation and loss of charge within a dielectric exposed to a GEO energetic flux environment (attenuated by a specified amount of shielding), using an equivalent Resistor-Capacitor (R-C) circuit model. The analysis demonstrated that repeated episodes of high electron flux (expected during the decline from solar max) could charge materials to charge densities and electric fields expected to cause electrical discharges, if the material had very high resistivity (and consequently a very long electrical time constant). So if the amount of shielding is defined and the key material properties are known, then a prediction of charging could be performed to determine if internal charging could plausibly produce ESD and cause the Inmarsat anomalies. However, because the design details for the two fleets are proprietary and unknown to the authors, a Bodeau-like analysis of the charging from launch to failure could not be performed for the hardware in each of the individual spacecraft. Instead, a typical RF amplifier system is surveyed in the next section to identify the most likely locations for charging and ESD (discussed in section 3). This is in preparation for a generic charging analysis to determine if sufficient fluence could be accumulated inside the key hardware to produce the failures (discussed in section 4).

3. RF Power Amplifier Systems

The increased anomaly rate following elevated energetic electron fluence over a period of 14 to 21 days prior to the anomalies suggests the failures may have been caused by (1) deep dielectric charging in materials with very high resistivity and long electrical time constants and (2) high electron flux exposure. Consequently, we investigate the components of the RF power amplifier system and their susceptibility to internal charging. The overall amplifier configuration consists of a coaxial cable that carries the RF signal to the amplifier input and another coaxial cable from the amplifier output to an antenna. Between the RF input and output of the SSPA are the transistors that are responsible for the power amplification and numerous passive components like resistors, switches, and capacitors.

Coaxial cables are made of an inner conductor, surrounded by an insulating dielectric layer surrounded by a conducting shield. There additionally may be an outer insulating dielectric jacket. The coaxial cables utilize

low-loss conductors, such as silver plated copper, and low-RF loss insulators (such as Teflon) to minimize the RF absorption at the operating frequency. The alternative to coax is waveguide, which has no insulator or floating center conductor, and therefore no ESD risk. Putting a coax and waveguide in series may DC isolate the coax center conductor at the interface. It is common practice to DC isolate the transistors by inserting a blocking capacitor before the transistor at the input and output coax interfaces. At high RF operating frequencies, the capacitor acts as a short circuit and freely passes the intended signal, while at lower frequencies, the capacitor has high impedance and blocks/reflects the undesired signal. The SSPAs also have a secondary power supply that converts the primary spacecraft power to the lower voltages needed to operate the internal circuits, and a command and telemetry section that is used to set the operating levels (e.g., gain) of the SSPA and to monitor operating levels (e.g., temperature, voltages, and RF power output). Since the telemetry from the failed units points to the RF circuitry as the location of the failure, we do not pursue the DC power and command and telemetry circuits as potential sources of the failure.

To assess the credibility of deep charging as a possible cause of the SSPA anomalies, we investigate the component of the amplifier system that is likely most exposed to charging: the coaxial cable, and the component most susceptible to experience voltages above their specified voltage ratings: the DC blocking capacitor. Other dielectrics and electrically isolated conductors within the SSPA RF section could potentially cause the anomalies. The spacecraft shielding around a coax cable and the SSPA it connects to should be the similar, so both would be exposed to similar electron flux levels. But the extra shielding provided by a typical unit chassis to potential ESD sources inside is greater (by at least 20 mils) than the shielding provided by the coax shield and outer jacket to the coax center conductor and internal dielectric. Consequently, the lower electron flux exposure inside a unit chassis makes potential ESD sources within a unit a less likely source of the anomalies.

Charging and discharging of the coax dielectric outer jacket was not of interest, since the internal RF transmission line is well isolated from an external electrical transient by the coax shield. The geometry and properties of the inner dielectric material control most of the electrical properties of the cable (e.g., impedance and RF loss). For RF applications, the dielectric material must have low loss. Teflon (polytetrafluoroethylene, PTFE) is a commonly used dielectric material for coax cables in satellite systems. Investigation of the possibility of internal charging of the dielectric material in the coax cables is provided in section 4.

The other component of RF communication system that may cause SSPA anomalies is the DC blocking capacitor. DC blocking capacitors are used to block the flow of DC current while passing desired RF signals and are typically found at the SSPA RF input and output connections to the coaxes. A typical DC blocking capacitor is a fixed single-layer microwave capacitor placed at the RF connection between a coax cable center conductor and field effect transistors (FETs) amplifier. Consequently, the coax center conductor may be DC isolated from ground by the blocking capacitors. A DC blocking capacitor is typically rated at 50 V to 100 V for safe operation, and in some cases is as low as 15 V. The voltage rating for safe operation is not the voltage at which absolute breakdown of the capacitor will occur, as one can operate the capacitor with AC signals of 100 V indefinitely and have little to no impact on the lifetime of the capacitor. The breakdown voltage of the DC blocking capacitor is unknown.

When the center conductor of the coax is isolated, internal charging within the coax cables in the communications system may charge the DC blocking capacitor to voltages exceeding their maximum voltage rating, compromising the capacitor and making it susceptible to failure. A fast transient breakdown of the blocking capacitor, plus isolated coax center conductor, would immediately cause overstress of the inner circuit components (e.g., most field effect transistors (FETs)) leading likely to failure and the consequent loss of RF output. The magnitude of damage depends on the energy released in the breakdown, as well as the voltage and current level and the duration of the breakdown.

In the subsequent analysis, the likelihood of internal charging for a typical Teflon-based RF coaxial cable is modeled and the voltage across the cable is quantified. The modeled voltages are compared to the voltage rating of the DC capacitor to assess whether the voltage across the cable is high enough to compromise or damage the DC blocking capacitor. If the cables experience a voltage that exceeds the rating of the DC blocking capacitor, an anomaly would likely occur.

Table 2. Material Properties of RG-141 Coaxial Cable [*International Telephone and Telegraph Corporation*, 1956; *MIL-C-17/170A*, 1985]

Class of Cable	High Temperature, Single Braid
Inner conductor	0.09 cm diameter silvered copper weld
Dielectric material	solid polytetrafluoroethylene (PTFE)-Teflon
Nominal diameter of dielectric	0.2946 cm
Protective covering	Polytetrafluoroethylene (Teflon)-tape moisture seal
Outer conductor diameter	0.371 cm (max)
Jacket	0.432 cm (max)
Nominal impedance	50.0 ohms
Nominal capacitance	28.5 picoFarads/ft
Maximum safe operating voltage	1900 Vrms

4. Internal Charging Analysis of the Coaxial Cables in SSPA System

In this section, we analyze the likelihood of internal charging in the coaxial cables leading to the power amplifiers as the cause of anomalies resulting from dielectric breakdown (induced electric field exceeds the breakdown threshold). The susceptibility of a material to internal charging depends on the flux and energy spectrum of the incident electrons and the material properties, specifically the conductivity, or bulk resistivity, and the electrical-decay time constant for the material [*Wrenn,* 1995; *Sorensen et al.,* 1999]. Prior tests of Teflon cables [*Green et al.,* 2009] showed that discharge pulses can occur from the coax cable outer insulation jacket but were not setup to measure charging or ESD pulses inside the coax. Other tests showed charging of coax cables with isolated center conductors up to multi kV levels, but no ESD occurred [*Payan et al.,* 2005].

The RF payloads in this study incorporate low-loss coaxial cables. Low-loss coaxial cables were used in the Fleet A and Fleet B payload designs, but the specific coax cables are unknown to the authors. RG-141 is a common RF coaxial cable with characteristics typical of low-loss RF coaxes generally (low-loss silver plated copper conductors with low-loss tangent Teflon inner dielectric), so it was used as a representative model for all RF cables. We analyze an RG-141 cable to determine if it is liable to breakdown due to internal charging in a worst-case GEO environment. The material properties of RG-141 are found in Table 2.

As shown in the table above, the maximum safe operating voltage for the coaxial cable is 1900 Vrms. The real breakdown threshold for the coaxial cable is not known but is expected to be greater than 1900 Vrms. The bulk conductivity of Teflon is typically cited at 1E-18/ohm m [*ASTM D257,* 2014] in air but ranges from 1E-20/ohm m [*Sessler and West*, 1975; *Bodeau,* 2010] to 1E-16/ohm m. Ionizing radiation creates additional electron-ion carriers in the material, which increases the conductivity. This Radiation-Induced Conductivity (RIC) depends upon the specific material and the radiation dose rate. The parameters that describe the RIC of PTFE are not well known and vary with aging (total dose) of the dielectric material [*Hanna et al.,* 2013]. This wide range of conductivities has been demonstrated experimentally as a result of radiation dose (and therefore, time on orbit). In addition, conductivity is a strong function of temperature. The SSPA temperature recorded in the acquired telemetry ranges from approximately 5 to 50°C. Coaxial cable temperature is not monitored, so the SSPA temperature range was used as estimation for the temperature range of the coaxial cable, with the additional inclusion of 0°C. In our analysis, we parametrically vary conductivity and temperature, covering conductivities 1E-16/ohm m to 1E-20/ohm m and temperatures of 0 to 50°C.

4.1. ESA's Internal Charging Tool—DICTAT

ESA's Internal Charging Tool, DICTAT (Dielectric Internal Charging Threat Analysis Tool), is used to determine if the coaxial cables leading to the power amplifiers are likely to experience breakdown [*Rodgers,* 2004]. DICTAT is a 1-D internal charging code that determines radiation transport through various shielding to identify the maximum internal electric field in a component on orbit and compares it with a suitable breakdown threshold to determine whether the component is susceptible to ESD. To determine this, DICTAT calculates the electron current using analytical approximations to quantify the electron transport through a shield and the charge deposited inside the dielectric. From this deposited charge, the maximum electric field within the dielectric is found. This field is then compared with the dielectric breakdown field. Assessments

Table 3. DICTAT Input Parameters for the Dielectric and the Conductor

Dielectric Parameters	Input to DICTAT
Dielectric material	Teflon
Thickness (cm)	0.1003
Density (g/cm^3)	2.17
Dielectric constant	2.15
Breakdown electric field (V/m)	1×10^7
RIC dose rate factor k_p	2E-14
Delta	0.695
Activation energy (eV)	1.4
Conductor parameters	Input to DICTAT
Shield material	copper
Shield thickness (cm)	0.077
Core material	copper
Core radius (cm)	0.047

of breakdown thresholds are generally empirical and vary widely. DICTAT has adopted a generic material-independent breakdown threshold value of 1×10^7 V/m, derived from *Frederickson* [1980] that is consistent with known experimental results and is commonly accepted.

DICTAT accounts for the effects of temperature (T) on bulk conductivity, σ_{bulk}, and the increase in radiation-induced conductivity $(\dot{D})$ as shown in equations (1) and (2) below. Equation (1) shows that the total conductivity is the sum of the bulk conductivity and the radiation-induced conductivity. The RIC dose rate factor, k_p, the power for the prompt radiation-induced conductivity, Δ, and the Arrhenius activation energy (the minimum energy required for a chemical reaction to occur), Ea, parameter are given in Table 3 in the next section. The other parameter is Boltzmann's constant, k_B.

$$\sigma(T, \dot{D}) = \sigma_{\text{bulk}}(\dot{T}) + k_p \cdot (\dot{D})^{\Delta} \tag{1}$$

$$\sigma_{\text{bulk}}(T) = \sigma_{\text{bulk}}(298K)^* \exp\left[\frac{-Ea}{k_B} \cdot \left(\frac{1}{T} - \frac{1}{298}\right)\right] \tag{2}$$

DICTAT divides the dielectric into "subzones" or layers of equal thickness and calculates the charge deposited within and the current passing through each zone. The code defines the "charging current" to be the net current flowing into each layer minus charge leakage out of the layer. The electric field is found at the boundary of each layer of the dielectric from the cumulative charge, and the surface voltage is found by summing the electric field for all zones.

The rate of charge leakage and electric field decay is controlled by the material's characteristic time constant, τ, which is defined as the product of the resistivity and dielectric constant. A wide range of electric time constants for Teflon are cited, ranging from fractions of an hour (0.9 h) [*Sorensen et al.,* 1999], to days (2.1 days) [*NASA-HDBK 4002A,* 2011], to almost a year (339 days) [*Swaminathan et al.,* 2003; *Sessler and West*, 1975]. However, these values are typically based on room temperature resistivity and no radiation-induced effects. DICTAT's approach is to take the total conductivity accounting for operating temperature and dose rate when calculating the conductivity of the dielectric (effective resistivity) and also when calculating the time constant. Since the dose rate is varying through the material, the conductivity, electrical time constant, and rate of charge leakage out of each layer vary. DICTAT derives the effective conductivity and time constant by integrating across the dielectric thickness. The DICTAT reports the charging time, which is the time it takes for the electric field that is enhanced from the environment, to decay to the equilibrium electric field.

4.2. DICTAT Simulations

The Fluence Model for Internal Charging (FLUMIC) is the worst-case electron environment model used in DICTAT. FLUMIC gives the integral electron spectra between an L shell, which describes the Earth's geomagnetic field lines, and particularly corresponds to the field line that crosses the Earth's magnetic equator at a value of R_E equal to the L parameter, of $L = 3$ and $L = 8$, and is valid for energies >200 keV [*Rodgers et al.,* 2004]. The AE8 model was not used, as it only provides the orbit-averaged spectrum rather than the worst-case spectrum. The FLUMIC model was found to overestimate the observed GOES >2 MeV integral electron flux by an average factor of 4 for the six time periods (1, 3, 7, 10, 14 to 21 days) prior to the anomalies, so the FLUMIC spectrum is assumed to be an appropriate worst-case spectrum for our analysis.

A cylindrical geometry is assumed, and the DICTAT default maximum field of view of 90° (hemispherical exposure) is selected. Table 3 provides a summary of the coaxial cable parameters input to DICTAT. The dielectric and shield thickness, shield and core material, and core radius were obtained from the material properties for the RG-141 coaxial cable. To account for aluminum spacecraft shielding, the outer copper

Table 4. DICTAT Results of the Maximum Electric Field, Charging Time (Days), and Peak Voltage for the 35 Simulations of Effective Conductivity, Bulk Resistivity and Temperature

DICTAT Input Parameters			DICTAT Derived Parameters		
Effective Conductivity (1/ohm m)	Bulk Resistivity at 25°C (ohm cm)	Temperature (°C)	E Max (V/m)	Charging Time (days)	Peak Voltage (V)
1E-16	1.00E + 18	0	3.87E + 06	1810	3393
1E-17	1.00E + 19	0	5.70E + 06	3170	5766
1E-18	1.00E + 20	0	6.12E + 06	3660	6567
1E-19	1.00E + 21	0	6.17E + 06	3730	6681
1E-20	1.00E + 22	0	6.18E + 06	3740	6694
1E-16	1.00E + 18	5	2.65E + 06	1125	2148
1E-17	1.00E + 19	5	5.11E + 06	2650	4890
1E-18	1.00E + 20	5	6.03E + 06	3540	6369
1E-19	1.00E + 21	5	6.16E + 06	3720	6658
1E-20	1.00E + 22	5	6.18E + 06	3740	6691
1E-16	1.00E + 18	10	1.56E + 06	599	1170
1E-17	1.00E + 19	10	4.19E + 06	2000	3744
1E-18	1.00E + 20	10	5.81E + 06	3280	5959
1E-19	1.00E + 21	10	6.14E + 06	3680	6600
1E-20	1.00E + 22	10	6.17E + 06	3740	6685
1E-16	1.00E + 18	20	3.62E + 05	122	243
1E-17	1.00E + 19	20	1.97E + 06	782	1519
1E-18	1.00E + 20	20	4.64E + 06	2290	4266
1E-19	1.00E + 21	20	5.94E + 06	3420	6182
1E-20	1.00E + 22	20	6.15E + 06	3700	6634
1E-16	1.00E + 18	30	6.64E + 04	21.6	43.5
1E-17	1.00E + 19	30	5.63E + 05	193	384.5
1E-18	1.00E + 20	30	2.59E + 06	1080	2073
1E-19	1.00E + 21	30	5.13E + 06	2650	4897
1E-20	1.00E + 22	30	6.04E + 06	3540	6382
1E-16	1.00E + 18	40	1.26E + 04	4.06	8.235
1E-17	1.00E + 19	40	1.22E + 05	39.7	80.04
1E-18	1.00E + 20	40	9.31E + 05	332	657.2
1E-19	1.00E + 21	40	3.40E + 06	1510	2864
1E-20	1.00E + 22	40	5.56E + 06	3030	5531
1E-16	1.00E + 18	50	2.70E + 03	0.842	1.765
1E-17	1.00E + 19	50	2.60E + 04	8.39	16.96
1E-18	1.00E + 20	50	2.47E + 05	80.3	161.3
1E-19	1.00E + 21	50	1.56E + 06	590	1156
1E-20	1.00E + 22	50	4.31E + 06	2060	3854

shielding is increased. A shielding thickness of 68 mils of Al was assumed for the spacecraft structure, which includes 4 mils aluminum shielding equivalent for a thermal blanket and the 28 mils of Al equivalent of a structural honeycomb panel. The total copper shielding input to DICTAT, 0.077 cm, is the outer copper shield surrounding the dielectric summed with the approximate contribution from spacecraft shielding—totaling to 0.077 cm (30.31 mils) of copper shielding or 100 mils of equivalent Al shielding. Typical values for the density, dielectric constant, RIC dose rate factor constant, delta constant, and thermal activation energy for Teflon electrical conductivity were also input [*Sessler*, 1979; *Frederickson et al.,* 1986; *NASA-HDBK 4002A,* 2011].

A total of 35 simulations were run, with a range of bulk resistivities taken at room temperature (1×10^{18}, 1×10^{19}, 1×10^{20}, 1×10^{21}, and 1×10^{22} ohm cm), and a range of operating temperatures (0°C, 5°C, 10°C, 20°C, 30°C, 40°C, and 50°C). The range of resistivities is chosen to cover the wide range of room temperature bulk resistivities quoted in literature, as discussed previously.

4.3. DICTAT Simulation Results

The comprehensive results from DICTAT for a single worst-case GEO orbit (1 day) are tabulated in Table 4, which includes the maximum electric field, charging time (in days), and peak voltage. There is a strong conductivity and temperature dependence for the maximum electric field, charging time, and voltage. As

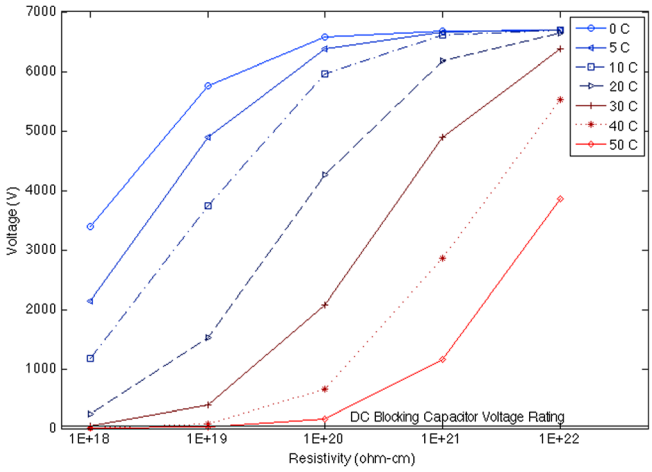

Figure 5. Voltage reached for 35 simulated scenarios of seven temperatures (0 to 50°C) and five room temperature resistivity values (1×10^{18} to 1×10^{22} ohm cm) for a single worst-case GEO orbit (~24 h).

conductivity decreases, we expect longer charging times, higher electric fields, and higher voltages. At higher temperatures, we expect shorter charging times, lower electric fields, and lower voltages. Figure 5 shows the voltage accumulated over 1 day for the range of Teflon room temperature resistivities (1×10^{18} to 1×10^{22} ohm cm), adjusted for operating temperatures between 0° and 50°C (per equation (1) above).

None of the cases exceeded the breakdown E field and corresponding voltage threshold of the dielectric material after 1 day, but the voltage exceeded the blocking capacitor maximum voltage rating for safe operation (>50 V) on 32 of 35 simulations. The voltage was <50 V for temperature of 30, 40, and 50°C at the highest room temperature conductivity of 1×10^{16}/ohm m (1×10^{18} ohm cm resistivity). The actual capacitor breakdown threshold, which should exceed the rated by a significant margin, is unknown.

4.4. Electric Field and Voltage Approximations After 1, 3, 7, 10, 14, and 21 Days

FLUMIC is inefficient to run for long time intervals. Therefore, the average electric field and accumulated voltage for the six periods of interest (1, 3, 7, 10, 14, 21 days) is approximated using the electric field and voltage values output from the DICTAT simulations for one orbit. The purpose of this analysis is to determine if hazardous voltages could be reached under any plausible subset of material properties. We assume that the worst-case flux and temperature are constant over the extended time period, so RIC, total conductivity, electrical time constant, and charge accumulated per day would remain constant.

To find the electric field beyond 1 day, we calculate the average electric field, E_0, of the 10 sections of the dielectric cylinder that DICTAT partitions for the first day. Ignoring charge leakage, each day would add an identical increment of trapped charge and increase the electric field by E_o. However, the accumulated charge and electric field from the previous day has exponentially decayed based on the time constant, τ. Table 4 tabulates the maximum E field of the 10 sections and the charging time. Using equation (3), along with the constant daily incremental electric field, E_0, charging time, τ, and orbit duration of 23.9 h, Δt, we determine the electric field for each day, n

$$E_n = E_{n-1}\left(\exp\frac{-\Delta t}{\tau}\right) + E_0 \tag{3}$$

The average electric field, $E_{n,}$ is then multiplied by the dielectric thickness, 0.1003 cm, to calculate the accumulated voltage. The accumulated electric field and voltages are tabulated in Tables 5 and 6, respectively, for periods of 1, 3, 7, 10, 14, and 21 days.

As expected, the largest accumulated electric fields and voltages occur for the trials with the lowest operating temperatures and lowest bulk room temperature conductivities (highest resistivities). The largest electric field, 1.32×10^8 V/m, occurred after 21 days at 0°C and a room temperature conductivity of 1E-20/ohm m. The electric field is greater than the dielectric breakdown threshold, 1×10^7 V/m; therefore, this trial, as well as all other trials, was liable to experience breakdown. The values in Table 6 that are bolded are greater than the maximum safe operating voltage (1900 Vrms) of the coaxial cable. A total of 161/210, or 76.7%, of the voltages in Table 6 were greater than 1900 V, which would indicate the coaxial cable was in an unsafe operation mode.

Table 5. DICTAT Results of Accumulated Electric Field After N Days

DICTAT Inputs		Average E Field After *N* Days					
Effective Conductivity (1/ohm m)	Temperature (°C)	1 day (V/m)	3 days (V/m)	7 days (V/m)	10 days (V/m)	14 days (V/m)	21 days (V/m)
1E-16	0	3.29E + 06	9.74E + 06	2.21E + 07	3.10E + 07	4.23E + 07	6.07E + 07
1E-17	0	5.75E + 06	1.71E + 07	3.93E + 07	5.56E + 07	7.67E + 07	1.12E + 08
1E-18	0	6.55E + 06	1.95E + 07	4.49E + 07	6.36E + 07	8.79E + 07	1.29E + 08
1E-19	0	6.66E + 06	1.99E + 07	4.57E + 07	6.47E + 07	8.95E + 07	1.31E + 08
1E-20	0	6.67E + 06	1.99E + 07	4.58E + 07	6.48E + 07	8.96E + 07	1.32E + 08
1E-16	5	2.14E + 06	6.29E + 06	1.41E + 07	1.95E + 07	2.62E + 07	3.67E + 07
1E-17	5	4.88E + 06	1.45E + 07	3.32E + 07	4.68E + 07	6.44E + 07	9.37E + 07
1E-18	5	6.35E + 06	1.89E + 07	4.36E + 07	6.16E + 07	8.51E + 07	1.25E + 08
1E-19	5	6.64E + 06	1.98E + 07	4.56E + 07	6.45E + 07	8.92E + 07	1.31E + 08
1E-20	5	6.67E + 06	1.99E + 07	4.58E + 07	6.48E + 07	8.96E + 07	1.32E + 08
1E-16	10	1.17E + 06	3.36E + 06	7.27E + 06	9.81E + 06	1.28E + 07	1.69E + 07
1E-17	10	3.73E + 06	1.11E + 07	2.52E + 07	3.54E + 07	4.84E + 07	6.97E + 07
1E-18	10	5.94E + 06	1.77E + 07	4.07E + 07	5.75E + 07	7.94E + 07	1.16E + 08
1E-19	10	6.58E + 06	1.96E + 07	4.52E + 07	6.39E + 07	8.83E + 07	1.30E + 08
1E-20	10	6.67E + 06	1.99E + 07	4.58E + 07	6.48E + 07	8.95E + 07	1.31E + 08
1E-16	20	2.43E + 05	6.07E + 05	1.02E + 06	1.17E + 06	1.28E + 06	1.34E + 06
1E-17	20	1.51E + 06	4.41E + 06	9.69E + 06	1.32E + 07	1.75E + 07	2.38E + 07
1E-18	20	4.25E + 06	1.26E + 07	2.89E + 07	4.06E + 07	5.57E + 07	8.06E + 07
1E-19	20	6.16E + 06	1.84E + 07	4.23E + 07	5.97E + 07	8.25E + 07	1.21E + 08
1E-20	20	6.61E + 06	1.97E + 07	4.54E + 07	6.43E + 07	8.88E + 07	1.30E + 08
1E-16	30	3.73E + 04	5.36E + 04	5.56E + 04	5.57E + 04	5.57E + 04	5.57E + 04
1E-17	30	3.84E + 05	1.02E + 06	1.91E + 06	2.34E + 06	2.72E + 06	3.06E + 06
1E-18	30	2.07E + 06	6.07E + 06	1.36E + 07	1.87E + 07	2.52E + 07	3.51E + 07
1E-19	30	4.88E + 06	1.45E + 07	3.33E + 07	4.69E + 07	6.45E + 07	9.38E + 07
1E-20	30	6.36E + 06	1.90E + 07	4.37E + 07	6.17E + 07	8.53E + 07	1.25E + 08
1E-16	40	1.13E + 04	1.13E + 04	1.13E + 04	1.13E + 04	1.13E + 04	1.13E + 04
1E-17	40	7.98E + 04	1.47E + 05	1.74E + 05	1.76E + 05	1.76E + 05	1.76E + 05
1E-18	40	6.55E + 05	1.83E + 06	3.73E + 06	4.84E + 06	5.99E + 06	7.35E + 06
1E-19	40	2.86E + 06	8.43E + 06	1.91E + 07	2.66E + 07	3.61E + 07	5.14E + 07
1E-20	40	5.51E + 06	1.64E + 07	3.77E + 07	5.32E + 07	7.34E + 07	1.07E + 08
1E-16	50	2.56E + 03	2.56E + 03	2.56E + 03	2.56E + 03	2.56E + 03	2.56E + 03
1E-17	50	2.07E + 04	2.20E + 04	2.20E + 04	2.20E + 04	2.20E + 04	2.20E + 04
1E-18	50	1.61E + 05	3.69E + 05	5.47E + 05	5.93E + 05	6.15E + 05	6.24E + 05
1E-19	50	1.15E + 06	3.32E + 06	7.17E + 06	9.67E + 06	1.26E + 07	1.66E + 07
1E-20	50	3.84E + 06	1.14E + 07	2.60E + 07	3.65E + 07	4.99E + 07	7.20E + 07

We acknowledge the nonrealistic aspect of using a short duration worst-case flux for multiweek time frames, and that we may be predicting voltages capable of breaking down the capacitors or even the coaxial cables in some cases when a more realistic environment could possibly not have such a risk. Given the uncertainty in material properties, the unknown capacitor breakdown voltage and our pessimistic environment, we deemed the analysis insufficient to *prove* a hazard existed. The results were sufficient motivation to undertake lab tests to assess risk.

Electron tests were conducted in collaboration with Space Systems/Loral (SSL) to better understand the implications of the high voltages reached inside the coaxial cable, and whether resulting damage would occur on the DC blocking capacitor. The next section describes the experiments in further detail.

5. High-Energy Electron Experiments With Coaxial Cable and a DC Blocking Capacitor

The Pelletron accelerator at NASA Marshall Space Flight Center, capable of emitting electrons from 300 keV to 2.5 MeV, was used to test a coax cable connected to an RF front-end circuit (DC blocking capacitor circuit). The accelerator is connected to a sample test chamber that is maintained below 1E-05 Torr (vacuum). Thick shielding inside the test chamber prevents electrons from ultimately discharging material inside the chamber other than the intended test sample. The overall goal of the test was to determine whether any

Table 6. DICTAT Results of Accumulated Voltage After N Days[a]

DICTAT Inputs		Accumulated Voltage After *N* Days					
Effective Conductivity (1/ohm m)	Temperature (°C)	1 day (V)	3 days (V)	7 days (V)	10 days (V)	14 days (V)	21 days (V)
1E-16	0	**3298.87**	**9.77E + 03**	**2.22E + 04**	**3.11E + 04**	**4.24E + 04**	**6.09E + 04**
1E-17	0	**5765.85**	**1.72E + 04**	**3.95E + 04**	**5.57E + 04**	**7.69E + 04**	**1.12E + 05**
1E-18	0	**6566.24**	**1.96E + 04**	**4.51E + 04**	**6.38E + 04**	**8.81E + 04**	**1.29E + 05**
1E-19	0	**6681.44**	**1.99E + 04**	**4.59E + 04**	**6.49E + 04**	**8.98E + 04**	**1.32E + 05**
1E-20	0	**6692.62**	**2.00E + 04**	**4.60E + 04**	**6.50E + 04**	**8.99E + 04**	**1.32E + 05**
1E-16	5	**2148.33**	**6.31E + 03**	**1.41E + 04**	**1.96E + 04**	**2.63E + 04**	**3.68E + 04**
1E-17	5	**4889.63**	**1.45E + 04**	**3.33E + 04**	**4.70E + 04**	**6.46E + 04**	**9.40E + 04**
1E-18	5	**6368.55**	**1.90E + 04**	**4.37E + 04**	**6.18E + 04**	**8.54E + 04**	**1.25E + 05**
1E-19	5	**6658.01**	**1.98E + 04**	**4.57E + 04**	**6.47E + 04**	**8.94E + 04**	**1.31E + 05**
1E-20	5	**6691.72**	**1.99E + 04**	**4.60E + 04**	**6.50E + 04**	**8.99E + 04**	**1.32E + 05**
1E-16	10	1169.97	**3.37E + 03**	**7.29E + 03**	**9.84E + 03**	**1.28E + 04**	**1.70E + 04**
1E-17	10	**3743.10**	**1.11E + 04**	**2.53E + 04**	**3.55E + 04**	**4.85E + 04**	**6.99E + 04**
1E-18	10	**5958.62**	**1.77E + 04**	**4.08E + 04**	**5.77E + 04**	**7.96E + 04**	**1.16E + 05**
1E-19	10	**6599.94**	**1.97E + 04**	**4.53E + 04**	**6.41E + 04**	**8.86E + 04**	**1.30E + 05**
1E-20	10	**6685.00**	**1.99E + 04**	**4.59E + 04**	**6.50E + 04**	**8.98E + 04**	**1.32E + 05**
1E-16	20	243.55	6.08E + 02	1.02E + 03	1.18E + 03	1.28E + 03	1.35E + 03
1E-17	20	1518.54	**4.42E + 03**	**9.72E + 03**	**1.33E + 04**	**1.76E + 04**	**2.39E + 04**
1E-18	20	**4266.16**	**1.27E + 04**	**2.89E + 04**	**4.07E + 04**	**5.59E + 04**	**8.09E + 04**
1E-19	20	**6181.79**	**1.84E + 04**	**4.24E + 04**	**5.99E + 04**	**8.27E + 04**	**1.21E + 05**
1E-20	20	**6633.84**	**1.98E + 04**	**4.55E + 04**	**6.44E + 04**	**8.91E + 04**	**1.31E + 05**
1E-16	30	37.36	53.8	55.8	55.8	55.8	55.8
1E-17	30	385.54	1.03E + 03	**1.92E + 03**	**2.35E + 03**	**2.73E + 03**	**3.06E + 03**
1E-18	30	**2072.90**	**6.08E + 03**	**1.36E + 04**	**1.88E + 04**	**2.52E + 04**	**3.52E + 04**
1E-19	30	**4896.65**	**1.46E + 04**	**3.34E + 04**	**4.70E + 04**	**6.47E + 04**	**9.41E + 04**
1E-20	30	**6382.39**	**1.90E + 04**	**4.38E + 04**	**6.19E + 04**	**8.55E + 04**	**1.25E + 05**
1E-16	40	11.28	11.3	11.3	11.3	11.3	11.3
1E-17	40	80.04	148	1.74E + 02	1.77E + 02	1.77E + 02	1.77E + 02
1E-18	40	657.19	1.84E + 03	**3.75E + 03**	**4.86E + 03**	**6.01E + 03**	**7.38E + 03**
1E-19	40	**2863.67**	**8.46E + 03**	**1.91E + 04**	**2.67E + 04**	**3.62E + 04**	**5.16E + 04**
1E-20	40	**5530.84**	**1.65E + 04**	**3.78E + 04**	**5.34E + 04**	**7.36E + 04**	**1.07E + 05**
1E-16	50	2.57	2.57	2.57	2.57	2.57	2.57
1E-17	50	20.80	22.1	22.1	22.1	22.1	22.1
1E-18	50	161.32	370	549	595	617	625
1E-19	50	1155.83	**3.33E + 03**	**7.19E + 03**	**9.70E + 03**	**1.26E + 04**	**1.67E + 04**
1E-20	50	**3854.43**	**1.14E + 04**	**2.61E + 04**	**3.66E + 04**	**5.01E + 04**	**7.23E + 04**

[a]The bold values designate quantities >1900 V, which is the voltage rating of the RG-141 for safe operation.

discharges were observed under irradiation, and if any damage was incurred as a result from breaching the voltage rating for safe operation of the DC blocking capacitor.

Payan et al. [2005] similarly tested coax cables with DC isolated ("floating") center conductors. In their test, a coax cable was charged to 1200 V (center conductor to shield) without spontaneous breakdown. The coax core was then switched to allow the current transient that occurred when the charge core was grounded to be measured. None of the SSPA failures we are assessing were associated with any commanded coax switching events. The lack of breakdown is consistent with the voltage rating of the RG-141 (1900 Vrms). Clearly, if a DC blocking capacitor had been attached to the coax, it would have experienced breakdown before the cable reached 1200 V. So we planned a charging test using an RG-141 coax connected with a DC blocking cap to determine if the coax would charge and cause the blocking cap to breakdown, and to measure the resulting current pulse (into a 50 ohms load) to determine if the pulse was sufficient to damage downstream RF components.

For the experiment presented in this study, a 2.18 m RG-141 coaxial cable rated to 1900 Vrms with a capacitance of 28.5 pF/ft (total capacitance of ~205 pF) and a DC blocking capacitor of ~15 pF rated to 50 V for safe operation were tested at two different electron beam energies (300 keV and 1 MeV). The lengths of coaxial cables vary significantly throughout the actual spacecraft, although satellite designers make every

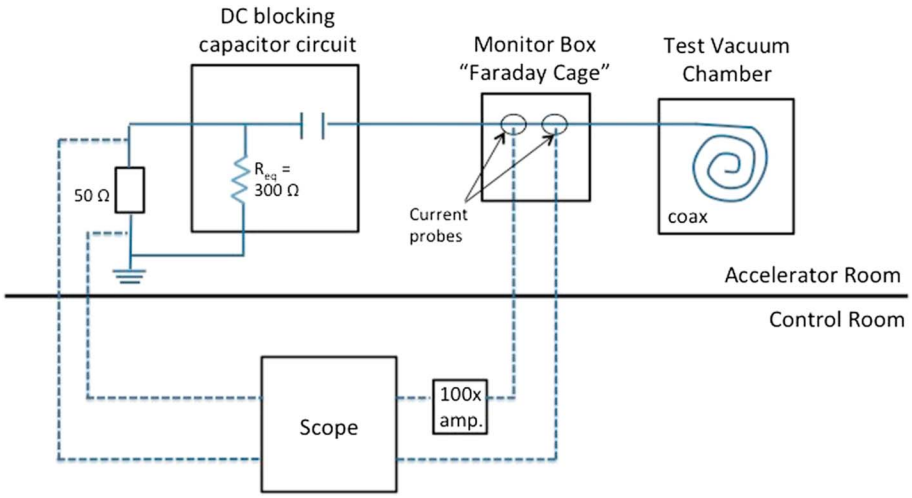

Figure 6. Test configuration for electron experiments for DC blocking capacitor and coaxial cable. Solid lines indicate RF flow of current. Dashed lines are probes where data are read by the scope.

attempt to minimize lengths to reduce loss, weight, and cost. A cable length of 2.18 m was chosen as representative of a typical coax length. The cable was exposed to a respective worst-case GEO test fluence for both energies. A beam energy of 300 keV primarily charges the dielectric in the vicinity of the coax shield, while a 1 MeV beam charges the dielectric closer to the center conductor. Worst-case GEO fluences of 3.6×10^{12} el/cm^2 for 300 keV and 8.4×10^{11} el/cm^2 for 1 MeV were reached using a flux of 1.9×10^8 el/cm^2/s (approximately 0.03 nA/cm^2).

A Pearson current probe was used to measure and record the total arc count, and a second current probe was used to monitor current on the coax. Arcs were defined by a trigger level of 20 mA across a 50 ohms resistor beyond the blocking capacitor. Figure 6 shows a diagram of the RF circuit test configuration that includes a flight-like chip blocking capacitor built on RF substrate that is common to GEO communications satellites. The coax is open at one end in the chamber; the center conductor of the other end of the coax connects directly to the DC blocking capacitor (the RF input) through a monitor box. Both the DC blocking capacitor and coaxial cable are electrically connected, and the center conductor of the coax and the input side of the blocking capacitor are at the same voltage. The coax shield is grounded at the chamber wall feedthrough. There is also another extension coaxial cable from the chamber wall to the monitor box. The outer shield of the extension coaxial cable is grounded at one end of the chamber wall, and the other end is connected to the monitor box chassis that is hard grounded to the facility ground, like the chamber wall. It is assumed that the in-orbit coaxes are an open circuit at both ends; however, the satellite SSPA manufacturers and satellite owners have not confirmed the assumption.

In the experiment, the electron beam strikes the coaxial cable, and charge begins to accumulate in the dielectric material and center conductor within the coax. As tested, most of the cable was in the electron beam since the coax was coiled. The charge accumulation results in a voltage between center conductor and shield and across the capacitor to the 50 ohms load. The monitor box is a Faraday cage through which the center conductor is routed, so that current probes can be used to measure current flowing along the center conductor. The current measurement is taken on the exposed center conductor of the coax and not around the shield of the coax.

A total of two arcs were observed, both at a beam energy of 1 MeV with a steady current of 0.03 nA/cm^2. The first arc occurred at 1.46×10^{11} el/cm^2 and had a peak of ~6 A and a duration of ~0.25 μs. This level and duration is similar to the findings of *Green et al.* [2009]. The second arc occurred at 2.35×10^{11} el/cm^2 had a ~4 A peak and lasted for ~0.25 μs. A visual inspection and a DC resistance check were performed after each arc. The corresponding peak voltages across the 50 ohms resistor reached 200 V and 300 V. The total pulse energy delivered to the 50 ohms would be up to ~200–450 uJ. The peak voltages and pulse energy are more than sufficient to damage the SSPA RF FETs (damage thresholds for FETs are cited at ~1 uJ in

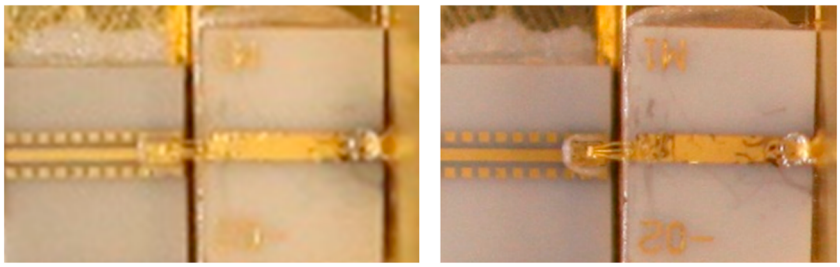

(a) (b)

Figure 7. High magnification of (a) pretest and (b) posttest articles. No burn marks appear on the posttest article.

Rudie et al. [1981] and *Davis and Gordon* [1992]): however, ESD pulse injection tests of the specific devices and circuits used in the SSPAs would be required to confirm this.

The RG-141 is rated to approximately 1.9 kVrms [*International Telephone and Telegraph Corporation,* 1956], far above the 50 V rating for safe operation of the DC blocking capacitor. The DC blocking capacitor represents $<$10% of the total capacitance of the RF circuit, so most of the stored charge and energy delivered by the breakdown comes from the coax, not the DC blocking capacitor. While the blocking capacitor can be considered the "weak link" from a voltage standpoint, it is the combined charge and energy that is being dumped and which would cause failure of downstream RF components.

Post arc inspections at the irradiation site revealed that after both arcs the blocking capacitor was still an open circuit from the RF input (coax connection) to the 50 ohms load and from the RF input to the facility ground. The equivalent resistor (R_{eq}) continued to show ~300 ohms to ground. An additional test was done with a Gohm-meter, which showed $>$20 Gohms across the coax shield to center conductor, indicating no degradation to the coax or the DC blocking capacitor, and no formation of a leakage path as a result of the discharge. One possible explanation why no damage occurred to the coax or DC blocking capacitor could be that energy of the transient arc was too low to cause visible damage. High magnification examination of the DC blocking circuit was challenging to capture due to lighting conditions, but is presented in Figure 7, which shows no damage or burn mark.

Postirradiation RF performance tests of the circuit were conducted by Space Systems/Loral (SSL) RF laboratory. Table 7 summarizes the preirradiation and postirradiation RF performance test results.

The posttest showed a 2 dB degradation in insertion loss and a 5 pF (33%) increase in the DC blocking capacitor, which is significant given that the precision of the measurement is better than 5% in capacitance. Insertion loss is a scattering parameter (S parameter), S12 parameter, used to describe the electrical behavior of electrical networks. Measurement of S12 parameter is performed using a network analyzer in a 50 ohms system. The 2 dB increase in insertion loss indicates resistive degradation occurred, even though it was not evident with visual inspection. The post RF measurement reconfirmed the operability of the RF blocking circuit and specifically that the DC blocking capacitor continued to isolate the input DC voltage applied to the RF input port. Visual inspection found no damage (e.g., broken or fused wire bond) nor discoloration on the thin film substrate. The result that there was a discharge suggests that a device following the capacitor (e.g., low-noise amplifier (LNA)) may have been the component that was most overstressed when the breakdown occurs.

Table 7. RF Performance Summary of Precharging and Postcharging Test

Time of Test	Frequency (GHz)	Insertion Loss (dB)	DC Blocking Capacitor (pF)
Pretest	5	−2.31	16.5 at 3 kHz
	10	−2.55	16.0 at 100 kHz
	15	−3.38	14.3 at 100 MHz
Posttest	5	−4.34	22.2 at 3 kHz
	10	−4.65	21.8 at 100 kHz
	15	−5.54	19.6 at 100 MHz

6. Summary and Conclusions

Lohmeyer and Cahoy [2013] assessed the role that space weather may have played in 26 high-power amplifier anomalies on GEO communications satellites. The additional results presented herein focused particularly on the role of the high-energy electron environment and possibility of internal charging as root cause of the anomalies. After calculating the >2 MeV electron fluence for periods of 1, 3, 7, 10, 14, and 21 days before anomalies, we find that the number of anomalies that occur after 14 days of >2 MeV electron fluence between 2×10^{10} and 4×10^{10} el/cm^2 is 2.62 standard deviations greater than 1000 Monte Carlo trials of 26 randomly selected anomaly dates, demonstrating the anomaly rate is well above a random failure rate. Similarly, we find that the number anomalies that occur after 21 days of >2 MeV electron fluence between 6×10^{10} and 8×10^{10} el/cm^2 are 2.34 standard deviations greater than 1000 Monte Carlo trials of 26 randomly selected anomaly dates, demonstrating the anomaly rate is well above a random failure rate.

The high correlation with 14 day and 21 day fluence suggests that deep charging may be occurring in materials with a long electrical charging time constant, which in turn requires a very high electrical resistivity. A survey of the RF payload design suggested that the RF coaxes connected to the SSPA inputs and outputs are the most likely source of ESD, because of the very high resistance dielectrics (PTFE Teflon) and high electron flux exposure. The coax center conductors were assumed to be DC isolated by DC blocking capacitors, commonly used at RF interfaces to coaxes.

DICTAT charging analysis with a bounding GEO electron flux environment predicted electrical breakdown over a wide range of operating temperatures and dielectric (room temperature) resistivities, lending credence to internal charging of the coax and DC blocking cap as a possible cause of the failures. Given the uncertainty in the coax and blocking capacitor properties and breakdown thresholds, we went the next step and conducted an electron beam test to show we could reach breakdown in a representative coax and DC blocking capacitor. The pulses delivered to a 50 ohms load, which were a substitute for the RF transistor next in line, were of sufficient voltage and energy to likely cause failure of the transistor. The combination of statistical correlation, charging analysis, and ground test shows that internal charging is a plausible explanation for at least some of the reported SSPA failures. We reach this conclusion based on the following factors: (1) the statistically significant elevated anomaly rate correlated with high 14 day and 21 day fluences preceding the anomalies; (2) the DICTAT analysis that predicts hazardous charging of a coax over a wide range of possible bulk resistivities and operating temperatures, (3) a demonstration by electron beam exposure that a representative coax (RG-141) isolated by a representative DC blocking circuit would discharge; and (4) the discharge peak voltage and energy appear more than sufficient to damage RF FETs.

To make the case that internal charging of RF coax was the root cause, more solid would require a much more detailed analysis using the specific coax connected to each SSPA, exposed to the specific flux inside the shielding provided by the specific satellite configuration, using the external electron flux environment accumulated following the unique launch dates of the eight satellites. This level of detail makes both the analysis and ground test prohibitively expensive. The authors suggest that internal charging is a sufficiently credible explanation of at least some of the SSPA failures that adopting the recommendation of *Payan et al.* to incorporate a shunt resistance to prevent charging of the coax and blocking cap appears to be a more practical investment.

Acknowledgments
The authors would like to thank Greg Ginet, Shu Lai, David Rodgers, Keith Ryden, and Kirk Laursen for their technical support, as well as Inmarsat for contributing the telemetry and technical guidance. The Inmarsat satellite telemetry is proprietary and thus cannot be distributed. However, the GOES electron data are publicly available at http://www.swpc.noaa.gov/ftpmenu/indices/old_indices_html. The authors would also like to acknowledge the Air Force Office of Sponsored Research (AFOSR) grant FA9550-13-1-0099 and the National Science Foundation (NSF) for funding this work through their Graduate Research Fellowship Program (GRFP).

References

ASTM Standard D257 (2014), *Standard Test Methods for DC Resistance or Conductance of Insulating Materials*, ASTM International, West Conshohocken, Pa., doi:10.1520/D0257.

Baker, D. N. (2000), The occurrence of operational anomalies in spacecraft and their relationship to space weather, *IEEE Trans. Plasma Sci.*, *28*(6), 2007–2016, doi:10.1109/27.902228.

Balcewicz, P. T., J. M. Bodeau, M. A. Frey, P. L. Leung, and E. J. Mikkelson (1998), Environment on-orbit anomaly correlation efforts at Hughes, 6th Spacecraft Charging Technology Conference.

Bodeau, J. M. (2010), High energy electron climatology that supports deep charging risk in GEO, paper AIAA 2010-1608 presented at 48th AIAA Aerospace Sciences Meeting Including the New Horizons Forum and Aerospace Exposition, Orlando, Fla., doi:10.2514/6.2010-1608.

Cotts, D. B., and Z. Reyes (1985), New polymeric materials expected to have superior properties for space-based use, SRI International, Menlo Park, Calif.

Davis, V. A., and L. W. Gordon (1992), *Spacecraft Surface Charging Handbook*, PL-TR-92-2232, Final Rep. ADA262778, Phillips Lab, Hanscomb AFB, Mass.

Denton, M. H., J. E. Borovsky, R. M. Skoug, M. F. Thomsen, B. Lavraud, M. G. Henderson, R. L. McPherron, J. C. Zhang, and M. W. Liemohn (2006), Geomagnetic storms driven by ICME- and CIR-dominated solar wind, *J. Geophys. Res.*, *111*, A07S07, doi:10.1029/2005JA011436.

Fennell, J. F., H. C. Koons, J. L. Roeder, and J. B. Blake (2001), Spacecraft charging: Observations and relationships to satellite anomalies, *Aerospace Rep. TR-2001(8570)-5*, Aerospace Corporation, Los Angeles, Calif.
Frederickson, A. R. (1980), Bulk charging and breakdown in electron irradiated polymers, in *Proceedings of the 3rd Spacecraft Charging Technology Conference, NASA Rep., 2182*, AIAA, New York.
Frederickson, A.R., D. B. Cotts, and J. A. Wall (1986), *Spacecraft Dielectric Material Properties and Spacecraft Charging*, AIAA Prog. in Astronaut. and Aeronaut., doi:10.2514/4.865817.
Green, N. W., A. R. Frederickson, and J. R. Dennison (2005), Experimentally Derived Resistivity for Dielectric Samples from the CRRES Internal Discharge Monitor, JAX-SP-05-001E, Japan Aerospace Exploration Agency (JAXA), Tsukuba, Japan, 4–8 April.
Green, N. W., H. Kirkham, W. Kim, and B. McAlpine (2009), Radiation dose testing on Juno high voltage cables, paper AIAA 2009-353 presented at 47th AIAA Aerospace Sciences Meeting, Orlando, Fla., doi:10.2514/6.2009-353, 5–8 Jan.
Hanna, R., T. Paulmier, P. Molinie, M. Belhaj, B. Dirassen, D. Payan, and N. Balcon (2013), Radiation induced conductivity in Teflon FEP irradiated with multienergetic electron beam, *IEEE Trans. Plasma Sci.*, *41*(12), 3520–3525, doi:10.1109/TPS.2013.2287097.
International Telephone and Telegraph Corporation (1956), *Reference Data for Radio Engineers*, 4th ed., pp. 606–611, Stratford Press Incorporated, New York.
Lai, S. T. (2012), *Fundamentals of Spacecraft Charging: Spacecraft Interactions With Space Plasmas*, Princeton Univ. Press, Princeton, N. J.
Lohmeyer, W. Q., and K. Cahoy (2013), Space weather radiation effects on geostationary satellite solid-state power amplifiers, *Space Weather*, *11*, 476–488, doi:10.1002/swe.20071.
MIL-C-17/170A (1985), Military specification sheet: Cables, radio frequency, flexible, coaxial, 50 ohms, U.S. Military.
Miyoshi, Y., and R. Kataoka (2008), Flux enhancement of the outer radiation belt electrons after the arrival of stream interaction regions, *J. Geophys. Res.*, *113*, A03S09, doi:10.1029/2007JA012506.
NASA-HDBK-4002A (2011), Avoiding problems caused by spacecraft on-orbit internal charging effects, NASA.
Payan, D., R. Reulet, and B. Diraseen (2005), Charging of coaxial lines with floating core at geosynchronous altitudes, paper JAXA-SP-05-001E presented at 9th Spacecraft Charging Technology Conference, Tsukuba, Japan, 4–8 April.
Reagan, J. B., R. E. Meyerott, E. E. Gaines, R. W. Nightingale, P. C. Filbert, and W. L. Imhof (1983), Space charging currents and their effects on spacecraft systems, *IEEE Trans. Electr. Insul.*, *EI-18*, 354–365, doi:10.1109/TEI.1983.298625.
Robinson, P. A. J. (1989), *Spacecraft Environmental Anomalies Handbook*, Final Rep. GL-TR-89-0222, Air Force Geophysics Laboratory, Hanscom AFB, Mass.
Roddy, D. (2001), *Satellite Communications*, 3rd ed., McGraw Hill, New York, doi:10.1036/0071382852.
Rodgers, D. J. (2004), *DICTAT Software: Users' Manual v3.0*, European Space Agency, Hamsphire, U. K.
Rodgers, D. J., K. A. Hunter, and G. L. Wrenn (2004), The FLUMIC electron environment model, Proceedings of the 8th Spacecraft Charging Technology Conference, Huntsville, Ala., 20–24 Oct.
Rudie, N. J., et al. (1981), Design support guide for radiation hardening of space electronic systems, IRT 6409-001, IRT Corp.
Sessler, G. M (Ed.) (1979), *Topics in Applied Physics*, vol. 33, Springer, New York.
Sessler, G. M., and J. E. West (1975), Electrets formed by low-energy electron injection, *J. Electrost.*, *1*(2), 111–123.
Shea, M. A., and D. F. Smart (1998), Space weather: The effects on operations in space, *Adv. Space Res.*, *22*(1), 29–38, doi:10.1016/S0273-1177(97)01097-1.
Sorensen, J., D. J. Rodgers, K. A. Ryden, P. M. Latham, G. L. Wrenn, L. Levy, and G. Panabiere (1999), ESA's tools for internal charging, in *IEEE Radiation and Its Effects on Components and Systems*, pp. 27–33, IEEE, Fontevraud, France, doi:10.1109/RADECS.1999.858540.
Swaminathan, P., A. R. Frederickson, J. R. Dennison, A. Sim, J. Brunson, and E. Crapo (2003), Comparison of classical and charge storage methods for determining conductivity of thin film insulators, in *Proceedings of the 8th Spacecraft Charging Technology Conference*, NASA Marshall Space Flight Center, Huntsville, Ala.
Vampola, A. L. (1987), Thick dielectric charging on high altitude spacecraft, *J. Electrost.*, *20*, 21–30, doi:10.1016/0304-3886(87)90083-0.
Wrenn, G. L. (1995), Conclusive evidence for internal dielectric charging anomalies on geosynchronous communications spacecraft, *J. Spacecr. Rockets*, *32*(3), 514–520, doi:10.2514/3.26645.
Wrenn, G. L., and R. K. Smith (1996), Probability factors governing ESD effects in geosynchronous orbit, *IEEE Trans. Nucl. Sci.*, *43*(6), 2783–2789, doi:10.1109/23.556867.